On the Calculation of the Free Surface Temperature of Gas-Tungsten-Arc Weld Pools from First Principles: Part II. Modeling the Weld Pool and Comparison with Experiments

R.T.C. CHOO, J. SZEKELY, and S.A. DAVID

By combining a mathematical model of the welding arc and of the weld pool, calculations are presented to describe the free surface temperature of weld pools for spot welding operations. The novel aspects of the treatment include the calculation of the heat and current fluxes falling on the free weld pool surface from first principles, a realistic allowance for heat losses due to vaporization, and a realistic allowance for the temperature dependence of the surface tension. The most important finding reported in this article is that the free surface temperature of weld pools appears to be limited by Marangoni convection, rather than heat losses due to vaporization. Furthermore, it was found that once thermocapillary flow can produce high enough surface velocities (>25 cm/s), the precise nature of the relationship between temperature and surface tension will become less important.

I. INTRODUCTION

IN Part I[1] we presented computed results describing the velocity and the temperature fields in welding arcs, together with the heat and current flux that falls on the weld pool surface. Indeed, the calculation of this heat and current flux was the principal objective of this work.

In Part II, we shall examine the behavior of the weld pool, which receives the energy and current flux from the welding arc, which has been described in Part I.[1] This treatment is thought to be more satisfactory than that described in earlier publications by the authors[2] and others,[3–7] because in the present case, we can represent the interaction between the welding arc and the weld pool, rather than specifying the boundary conditions for the energy and the current flux independently, as has been done in the past.

As a result of previous weld pool modeling efforts,[2–7] it has been established that weld pool circulation, and hence, heat transfer in weld pools, is governed by electromagnetic forces, by buoyancy forces, by arc drag, and also by thermocapillary forces—the latter being dominant in most cases. Since thermocapillary motion is essentially driven by the temperature gradients at the free surface of the weld pool, the precise knowledge of this temperature profile is critical. In the calculations to be presented in the following, we shall be able to address this problem meaningfully, by carefully calculating both the heat flux falling on the free surface (through the solution of the previously developed arc equations) and the heat loss by vaporization. Furthermore, in computing the thermocapillary forces, use will be made of the most recently developed relationships.

R.T.C. CHOO, Research Associate, is with the Department of Metallurgy and Materials Science, University of Toronto, Toronto, ON M5S 1A4, Canada. J. SZEKELY, Professor, is with the Department of Materials Science and Engineering, Massachusetts Institute of Technology, Cambridge, MA 02139. S.A. DAVID, Group Leader, is with the Metals and Ceramics Division, Oak Ridge National Laboratory, Oak Ridge, TN 37381.

Manuscript submitted June 10, 1991.

In Section II, we shall present the mathematical formulation, while the computed results will be presented in Section III; these latter will include a critical comparison with measurements. The discussion is contained in Section IV.

II. MATHEMATICAL FORMULATION OF THE WELD POOL

The gas tungsten arc welding (GTAW) process is shown schematically in Figure 1. The arc is struck between the electrode (cathode) and the workpiece (anode); thus, thermal energy is transferred to the anode, which will raise the temperature of the surface, and a molten pool develops. This pool will grow until the heat input equals the heat loss by radiation, convection, conduction, and vaporization. The recirculating flow field in the pool is driven by a combination of buoyancy, Lorentz ($J \times B$), and surface tension forces. The complex transport phenomena that occur in the system are summarized in Figure 1.

The mathematical representation of this problem has to include the following physical processes that govern the weld pool behavior:

(1) fluid flow in the weld pool;
(2) heat transfer in the weld pool;
(3) melting and solidification phenomena;
(4) transient heat conduction into the workpiece; and
(5) heat-transfer phenomena at the free surface.

In the statement of the problem, the following major assumptions are made:

(1) the system is axisymmetric;
(2) the property values are independent of temperature (except for the temperature-dependent surface tension);
(3) transient behavior is considered; and
(4) melt circulation is driven by the combination of thermocapillary, buoyancy, and electromagnetic forces.

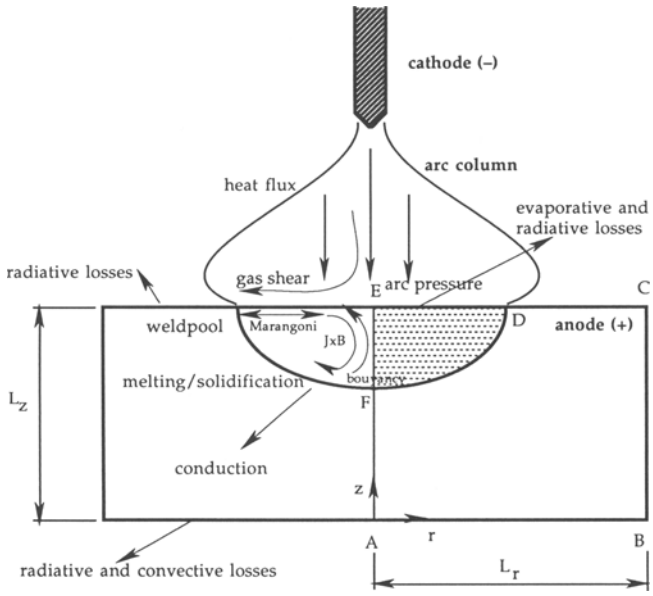

Fig. 1—Schematic representation of combined gas tungsten arc and weld pool phenomena. The left portion indicates the various physical phenomena occuring within the workpiece, while the right portion shows the computational domain. The origin for the weld pool is at point e, while the origin for the welding arc is at point E.

A. *Governing Equations*

Then the governing equations take the following form:

Conservation of mass

$$\frac{\partial u}{\partial r} + \frac{u}{r} + \frac{\partial w}{\partial z} = 0 \qquad [1]$$

Conservation of radial momentum

$$\frac{\partial u}{\partial t} + u\frac{\partial u}{\partial r} + w\frac{\partial u}{\partial z} = -\frac{1}{\rho}\frac{\partial P}{\partial r} + \nu\left[\frac{\partial^2 u}{\partial r^2} + \frac{1}{r}\frac{\partial u}{\partial r} - \frac{u}{r^2} + \frac{\partial^2 u}{\partial z^2}\right] - \frac{1}{\rho}(J_z B_\theta) - \frac{1}{\rho}Ku \qquad [2]$$

(transient) + (convective) = (pressure gradient) + (diffusive) + (Lorentz) + (drag)

Conservation of axial momentum

$$\frac{\partial w}{\partial t} + u\frac{\partial w}{\partial r} + w\frac{\partial w}{\partial z} = -\frac{1}{\rho}\frac{\partial P}{\partial z} + \nu\left[\frac{\partial^2 w}{\partial r^2} + \frac{1}{r}\frac{\partial w}{\partial r} + \frac{\partial^2 w}{\partial z^2}\right] + \frac{1}{\rho}(J_r B_\theta) - \frac{1}{\rho}Kw + g\beta(T - T_r) \qquad [3]$$

(transient) + (convective) = (pressure gradient) + (diffusive) + (Lorentz) + (drag) + (buoyancy)

Conservation of thermal energy

$$\frac{\partial T}{\partial t} + u\frac{\partial T}{\partial r} + w\frac{\partial T}{\partial z} = \alpha\left[\frac{\partial^2 T}{\partial r^2} + \frac{1}{r}\frac{\partial T}{\partial r} + \frac{\partial^2 T}{\partial z^2}\right] - \frac{\Delta H}{\rho C_p}\frac{\partial f_L}{\partial t} \qquad [4]$$

(transient) + (convective) = (diffusive) + (latent heat)

B. *Source Terms and Auxiliary Phenomenological Equations*

1. *Melting and solidification modeling*

The temperature-dependent drag term which represents fluid flow in the mushy zone is incorporated into the momentum equation *via* $-Ku$ and $-Kw$ where

$$K = \begin{cases} 0 & T > T_{liq} \\ K_{max}(T_{liq} - T)/(T_{liq} - T_{sol}) & T_{sol} \le T \le T_{liq} \\ \infty & T < T_{sol} \end{cases} \qquad [5]$$

The latent heat term is added to the energy equation *via* $-(\Delta H_L\, \partial f_L/C_p\, \partial t)$ where

$$f_L = \begin{cases} 1 & T > T_{liq} \\ (T - T_{sol})/(T_{liq} - T_{sol}) & T_{sol} \le T \le T_{liq} \\ 0 & T < T_{sol} \end{cases} \qquad [6]$$

The term f_L, defined as the fraction of liquid, has been linearized for simplicity. It can be used to simulate true volume fraction liquid if the phase diagram of the alloy is known. This model is being used in the commercial fluid flow and heat-transfer package FLOW-3D (Flow Science of Los Alamos).[8]

2. *Electromagnetic source terms*

The continuity equation for electric charge and current is given by Gauss' law as

$$\nabla \cdot \underline{J} + \frac{\partial \rho_c}{\partial t} = 0 \qquad [7]$$

where ρ_c is the charge density. If the electric field is assumed to be quasi-steady state, then the continuity equation becomes

$$\nabla \cdot \underline{J} = 0 \qquad [8]$$

From Ohm's law (assuming the magnetic Reynolds number is much less than unity[9]),

$$\underline{J} = \sigma_e \underline{E} \qquad [9]$$

and since the scalar electric potential, ϕ, is defined as $\underline{E} = -\nabla\phi$, Eqs. [8] and [9] can be combined to give

$$\nabla^2\phi = \frac{1}{r}\frac{\partial}{\partial r}\left(r\frac{\partial \phi}{\partial r}\right) + \frac{\partial^2 \phi}{\partial z^2} = 0 \qquad [10]$$

assuming that the electrical conductivity is constant for

steel. This is the standard Laplace equation for electrical charge continuity.

The current density is calculated from

$$J_r = -\sigma_e \frac{\partial \phi}{\partial r} \qquad [11]$$

$$J_z = -\sigma_e \frac{\partial \phi}{\partial z} \qquad [12]$$

while the self-induced azimuthal magnetic field is derived from Ampere's law as

$$B_\theta = \frac{\mu_0}{r} \int_0^r J_z \, r \, \partial r \qquad [13]$$

The integration constant is assumed zero since $B_\theta \rightarrow 0$ as $r \rightarrow 0$ as the integrand approaches zero. The Lorentz force, $\underline{J} \times \underline{B}$, is then given by

$$\underline{J} \times \underline{B}|_r = -J_z B_\theta \qquad [14]$$

$$\underline{J} \times \underline{B}|_z = J_r B_\theta \qquad [15]$$

3. *Effect of mass-transfer control vaporization*

As discussed in an earlier article,[10] the rate of mass transfer from the welding arc is controlled by the combined effect of Langmuir vaporization and mass transfer in the anode concentration boundary layer. Figure 2 illustrates this effect schematically whereby the rate of mass loss is described by an effective mass-transfer coefficient:

$$m_{\text{Mn}} = h_{m(\text{eff})} \, \Delta C = h_{m(\text{eff})} \, [C^s_{\text{Mn}} - C^\infty_{\text{Mn}}] \qquad [16]$$

where

$$\frac{1}{h_{m(\text{eff})}} = \frac{1}{h_{\text{vap}}} + \frac{1}{h_{\text{mass}}} \qquad [17]$$

Experimental studies by Block-Bolten and Eagar[11] indicated that the two dominant vapor species in the welding of steel are Fe and Mn. Only these two elements will be considered in the vaporization analysis. Iron and manganese are dominant because of their high vapor pressures. The discussion that follows will consider Mn as the vapor species, although it is implicit that similar treatment is given to Fe.

a. *Derivation of mass-transfer coefficient due to vaporization*

The Langmuir vaporization rate is given by

$$m_{L,\text{Mn}} = \frac{M_{\text{Mn}} P_{\text{Mn}}}{\sqrt{2\pi M_{\text{Mn}} \text{R} T}} \qquad [18]$$

The value of h_{vap} is obtained from Eq. [18] by assuming $P_{\text{Mn}} = C^s_{\text{Mn}} \text{R} T$ and $C^\infty_{\text{Mn}} = 0$ in the bulk of the shielding gas

$$h_{\text{vap}} = \frac{\text{R} T}{\sqrt{2\pi M_{\text{Mn}} \text{R} T}} \qquad [19]$$

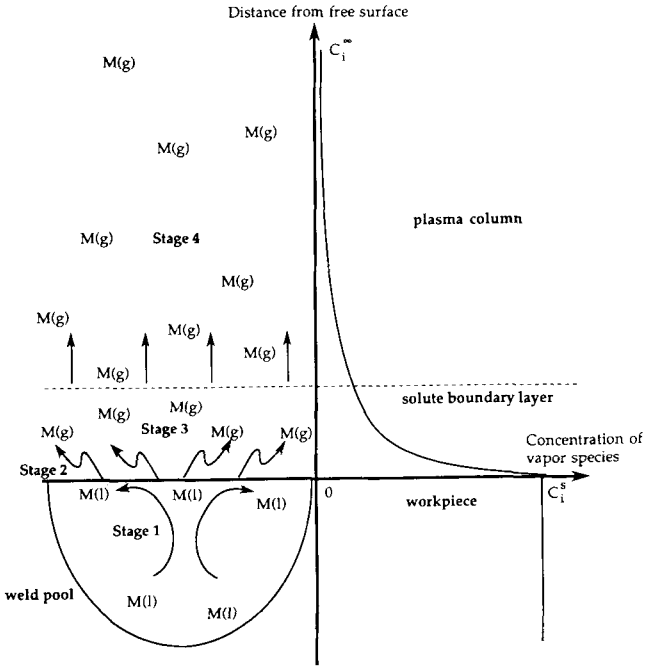

Fig. 2—Vaporization stages of gaseous species from the weld pool surface. The diagram on the left shows the mechanisms by which the high vapor pressure species escape from the weld pool, while the diagram on the right shows the concentration profile of that vapor species as a function of distance from the free surface. Stage 1: convected to the free surface by fluid flow circulation; stage 2: vaporized from the free surface; stage 3: diffused across the concentration boundary layer; and stage 4: transported away by the carrier gas.

b. *Derivation of mass-transfer coefficient due to diffusion*

McKelliget and Szekely[12] employed a convection correlation for a stagnation point flow over a flat surface as given by the following equations:

$$\frac{\text{Nu}_w}{\sqrt{\text{Re}_w}} = 0.515 \left(\frac{\mu_e \rho_e}{\mu_w \rho_w} \right)^{0.11} \qquad [20]$$

$$Q_{a.\text{conv}} = \left(\frac{\text{Nu}_w}{\sqrt{\text{Re}_w}} \right) \frac{(h_e - h_w)}{\text{Pr}_w} \sqrt{\mu_w \rho_w \frac{\partial u_e}{\partial r}} \qquad [21]$$

Rewriting Eqs. [20] and [21] and modifying $\partial u_e / \partial r$,

$$q_{\text{conv}} = 0.515 \left(\frac{\mu_e \rho_e}{\mu_w \rho_w} \right)^{0.11} \sqrt{\mu_w \rho_w \frac{u_e}{r}} \left[\frac{\overline{C_p}}{\text{Pr}_w} \right] [T_e - T_w] \qquad [22]$$

where $\overline{C_p}$ is the integral mean heat capacity given by

$$\overline{C_p} = \frac{1}{T_e - T_w} \int_{T_w}^{T_e} C_p \, dT \qquad [23]$$

Equation [22] can be written as $q = h_{\text{heat}} \, \Delta T$; thus,

$$h_{\text{heat}} = 0.515 \left(\frac{\mu_e \rho_e}{\mu_w \rho_w} \right)^{0.11} \sqrt{\mu_w \rho_w \frac{u_e}{r}} \left[\frac{\overline{C_p}}{\text{Pr}_w} \right] \qquad [24]$$

Equations [20] and [21] were originally obtained from a heat-transfer correlation for jet flow from a rocket nozzle impinging onto a flat surface.[13,14] Using the analogy between mass transfer and heat transfer, the mass-transfer coefficient is given by

$$\frac{h_{heat}}{h_{mass}} = \overline{\rho C_p \left[\frac{Sc}{Pr}\right]^n} \quad [25]$$

where

$$\text{Pr, Prandtl Number, } = \frac{C_p \mu}{k} \quad [26]$$

$$\text{Pr}_w\text{, Prandtl Number at anode surface, } = \left[\frac{C_p \mu}{k}\right]_{surf} \quad [27]$$

$$\text{Sc, Schmidt Number, } = \frac{\nu}{D_{Mn\text{-}Ar}} \quad [28]$$

and $n \sim 0.6$ for flat surfaces. The terms at the right side of Eq. [25] are the integral mean quantities using an expression of the type given in Eq. [23]. The diffusivity in the Schmidt number is calculated from the Chapman-Enskog relationship.[15] The Lennard-Jones parameters ε's and σ's are estimated using the melting point data for the metallic species and the boiling point data for the gaseous species.

A major assumption is invoked in that the concentration of Mn at the free surface is described by its equilibrium partial pressure, which is a function of temperature. This assumption is routinely employed in surface kinetics. Letting $C^s_{Mn} = P_{Mn}/RT_s$, P_{Mn} may be described by the thermodynamic relationship

$$a_{Mn} = \frac{P_{Mn}}{P^0_{Mn}} \quad [29]$$

or

$$\log P_{Mn(T_s)} = \log a_{Mn(T_s)} + \log P^0_{Mn} \quad [30]$$

For a binary alloy, the activity of Mn at temperature T_s can be calculated from the Gibbs-Helmholtz relationship where

$$\log a_{Mn(T_s)} = \log a_{Mn(T_{ref})} + \frac{\overline{\Delta G^{xs}}Mn}{4.575}\left(\frac{1}{T_s} - \frac{1}{T_{ref}}\right) \quad [31]$$

The data for $aMn(T_{ref})$ and $\overline{\Delta G^{xs}}$ Mn are given by Hultgren *et al.*[16] The binary solution is assumed to be regular such that $\overline{\Delta G^{xs}}$ Mn $= \Delta H_{mix,Mn}$ and is independent of temperature. This assumption is generally valid for steel. The heat loss by vaporization is thus given as

$$q_{vap,tot} = m_{Fe} L_{vap,Fe} + M_{Mn} L_{vap,Mn} \quad [32]$$

and the net heat flux at the liquid surface (region DE in Figure 1) is thus

$$q_{net} = q_a - q_{vap} \quad [33]$$

The radiative heat loss at the anode surface is already embedded into the q_a term.

C. *Weld Pool Boundary Conditions*

1. *Boundary conditions for momentum*

The momentum boundary conditions are given by the second and third column in Table I; these are the standard expressions specifying zero velocity at the solid surface, symmetry, and the continuity of shear stress at the free surface. At the free surface (region DE), Marangoni or surface tension-driven flow is described by

$$\tau_{st} = \mu_{liq}\left(\frac{\partial u}{\partial z}\right)_{liq} = \left(\frac{\partial \gamma}{\partial T}\right)\left(\frac{\partial T}{\partial r}\right) \quad [34]$$

The temperature-dependent surface tension is obtained from a semi-empirical treatment given by Sahoo *et al.*[17] as

$$\frac{\partial \gamma}{\partial T} = -A - R\Gamma_s \ln(1 + K_{seg} a_s) - \frac{K_{seg} a_s}{1 + K_{seg} a_s}\frac{\Gamma_s \Delta H^\circ}{T} \quad [35]$$

where

$$K_{seg} = k_1 \exp\left(\frac{-\Delta H^\circ}{RT}\right) \quad [36]$$

Table I. Boundary Conditions for Workpiece

Region	u	w	T	ϕ
AB	0	0	$\frac{\partial T}{\partial z} = 0$ or $T = 288$ K	$\frac{\partial \phi}{\partial z} = 0$
BC	0	0	$\frac{\partial T}{\partial r} = 0$ or $T = 288$ K	0
CD	0	0	$-k\frac{\partial T}{\partial z} = -q_a$	$J_a = -\sigma_e \frac{\partial \phi}{\partial z}$
DE	$\mu \left.\frac{\partial u}{\partial z}\right\|_{liq} = \left(\frac{\partial \gamma}{\partial T}\right)\left(\frac{\partial T}{\partial r}\right)$	0	$-k\frac{\partial T}{\partial z} = -q_a + q_{vap}$	$J_a = -\sigma_e \frac{\partial \phi}{\partial z}$
EF	0	$\frac{\partial w}{\partial r} = 0$	$\frac{\partial T}{\partial r} = 0$	$\frac{\partial \phi}{\partial r} = 0$
FA	0	0	$\frac{\partial T}{\partial r} = 0$	$\frac{\partial \phi}{\partial r} = 0$

2. *Boundary conditions for thermal energy*

These are necessarily specific to the given application; in the present work, we shall examine two particular cases, namely:

(1) reproducing the earlier computed results by Oreper and Szekely,[2] in order to test the internal consistency of the model, and
(2) perform calculations that correspond to the experimental conditions reported by Kraus[19] and Zacharia *et al.*[20]

a. *The theoretical model of Oreper and Szekely[2]*

The primary purpose here is to provide a comparison with earlier work.[2] The heat flux is assumed to obey a Gaussian-type distribution of the form

$$q_a = q_0 \exp(-\alpha_q r^2) \quad [37a]$$

$$= 6.135 \times 10^7 \exp(-10^5 r^2) \quad [37b]$$

$\Rightarrow$ (such as in Reference 2) while zero flux is assumed at the walls:[2]

$$\frac{\partial T}{\partial z} = 0 \quad \text{at } z = 0 \quad [38]$$

$$\frac{\partial T}{\partial r} = 0 \quad \text{at } r = L_r \quad [39]$$

Equation [37b] is for a "cathode-spot" mode of operation. This heat flux distribution is estimated for a 6.3-mm arc at 200 A by Nestor.[18]* Furthermore, the maximum temperature is not allowed to exceed 2500 K.

*Private communication with Dr. G.M. Oreper of Northern Research, Waltham, MA.

b. *Kraus' experimental temperature results[19] and Zacharia et al.'s weld pool results[20]*

The second case is used as a test of the current model against experimental results. The reader is referred to Kraus[19] and Zacharia *et al.*[20] for details of the experimental arrangement. Kraus[19] performed the surface temperature measurements, while Zacharia *et al.*[20] carried out the weld bead tests.

The heat flux is calculated using the transport equations described in Part I.[1] Comparison between calculated and experimentally measured heat and current fluxes for the welding arc have been performed elsewhere[21,22] and are not repeated here. The sides and the bottom of the plate are assumed isothermal at 288 K due to the use of a water-cooled copper plate. The preweld arc gap in Kraus' experiments[19] was 2.0 mm, but because of the liquid dome that forms due to the thermal expansion of the fluid which is 0.41-mm high, the effective arc length employed here is 1.5 mm.

Finally, symmetry conditions are assumed at regions EF and FA, as seen in Figure 1. The location of region DF is calculated from the energy equation using a latent heat source term for the phase change. This front is transient and needs to be evaluated at each time step.

3. *Electric potential boundary conditions*

The boundary conditions (BCs) shown in column 5 of Table I are quite straightforward. The selection of an isopotential line ($\phi = 0$) at BC is such that the right wall is far away from the weld pool such that $J_z \sim 0$ in this region.

As in the case of the thermal boundary conditions described above, two types of current fluxes are employed. The first case corresponds to the exponential heat flux distribution given by Oreper and Szekely[2] for a cathode spot operation as

$$J_a = J_0 \exp(-\alpha_j r) = 5.11 \times 10^6 \exp(-230\, r) \quad [40]$$

while the second is calculated using the transport equations described in Part I[1] in conjunction with the input process parameters.

D. *Material Properties for the Weld Pool*

Tables II and III list the transport properties and the input parameters for the weld pool calculations performed in this study. Table IV lists the composition of the workpiece employed by Kraus.[19] The size of the plate used by Oreper and Szekely[2] has a radius of 20 mm and a thickness of 12.7 mm, while that used by Kraus[19] is a rectangular block (40 by 40 by 12.5 mm). The heat source is assumed to be located at the center of the plate.

E. *Solution Technique*

The numerical package PHOENICS[23] was used to solve the transport equations. This is a commercial finite domain three-dimensional code based on the SIMPLE algorithm.[24] Uniform grids were employed in the molten zone. Variable grids were employed in the solid region, where they increased geometrically in size at no more than 15 pct increments. In most calculations, there were at least 200 nodes in the molten zone during steady state. The minimum radial grid was 0.15 mm, while the minimum axial grid was 0.075 mm. The size of the weld pool was of the order of 4 mm. The above grid configuration, with uniform grids in the molten zone and variable grids in the solid zone, was selected on the basis of exhaustive grid sensitivity trials and computer economy.

Grids sensitivity trials were made by first selecting a uniform cell size (0.50-mm radial and 0.40-mm axial) for the entire domain. This configuration was commonly used by many early modelers. Variable grids were then employed in the solid zone for a second grid configuration. It was found that the computed results of temperature, velocities, and electric potential at $t = 5$ seconds real time simulation were virtually identical for the two cases.

Subsequently, the cell size in the molten zone was reduced by 50 pct and later by 25 pct when finer grids (<0.15 mm) were used. In all cases, the transition from the uniform grids to the variable grids beyond the solid-liquid interface was done gradually at 10 pct increments. This process was repeated each time the grids in the molten zone were reduced. Grid insensitivity was determined when two sets of computed results for two different grid configurations differed by no more than 5 pct. The above arrangement was chosen on that basis.

Convergence is achieved when the spot values of temperature, pressure, and velocities at the critical location, which is the second node under the free surface adjacent

Table II. Material Properties and Workpiece Information of AISI 304[2,5,17,19,21]

Nomenclature	Symbol	Value
Activity of sulfur	a_s = [S]	0.022 wt pct
Atomic weight (Ar)	M_{Ar}	39.948 g/mole
Atomic weight (Fe)	M_{Fe}	55.847 g/mole
Atomic weight (Mn)	M_{Mn}	54.938 g/mole
Boiling point (Ar)	$T_{bp(Ar)}$	87.2 K
Coefficient of thermal expansion	β	10^{-4} K^{-1}
Constant in surface tension coefficient	A	4.3×10^{-4} N/m · K
Density (steel)	ρ	7,200 kg/m^3
Density (Ar)	ρ_{Ar}	1,400 kg/m^3
Density (Fe)	ρ_{Fe}	7,020 kg/m^3
Density (Mn)	ρ_{Mn}	6,430 kg/m^3
Electrical conductivity (steel)	σ_e	7.14×10^5 Ω^{-1}m^{-1}
Emissivity	ε	0.4
Function of entripy of segregation	k_1	3.18×10^{-3}
Gas constant	R	8314.3 J/kg · mole
Heat capacity (steel)	C_p	753 J/kg · K
Latent heat of fusion (steel)	ΔH	2.47×10^5 J/kg
Latent heat of vaporization (Fe)	$L_{vap,Fe}$	6.091×10^6 J/kg
Latent heat of vaporization (Mn)	$L_{vap,Mn}$	4.0135×10^{-6} J/kg
Liquidus temperature (steel)	T_{liq}	1523 K
Melting point (Fe)	$T_{mp(Fe)}$	1809 K
Melting point (Mn)	$T_{mp(Mn)}$	1518 K
Permeability of free space	μ_0	1.26×10^{-6} H/m
Plate thickness	L_z	12.5 mm
Plate radius	L_r	20 mm
Reference temperature for Table III	T_{ref}	1819 K
Solidus temperature (steel)	T_{sol}	1723 K
Standard heat of adsorption	ΔH°	-1.88×10^8 J/kg · mole
Stefan-Boltzmann constant	σ_b	5.67×10^{-8} W/m^{2}K^4
Surface excess at saturation	Γ_s	1.3×10^{-8} J/(kg · mole) · m^2
Thermal conductivity (liquid steel)	K_{liq}	20 W/m · K
Thermal conductivity (solid steel)	k_{sol}	20 W/m · K
Viscosity	μ	0.006 kg/m · s

to the z-axis, remain unchanged (<0.1 pct) while the residuals of the continuity, momentum, and energy equations continue to decrease. The spot value is normally selected as the location which is the last to converge, that is, the spot of slowest convergence. As the free surface is the region with the strongest driving force, monitoring the spot value in that location seems logical. In general, the residuals must decrease by at least three orders of magnitude with respect to the first sweep before the run was terminated. This was because by that time, the field values did not change significantly (<0.1 pct) with each subsequent sweep. In most production runs, the residuals decreased by four to six orders of magnitude with respect to the first sweep.

The computations were done on engineering workstations (VAXSTATIONS* 3100/30 and 3100/38) and on the APOLLO DN 10000 computer. It took about 6 hours on the Apollo for each second of real-time simulation using a 40 × 41 irregular grid configuration.

*VAXSTATION is a trademark of Digital Equipment Corporation, Maynard, MA.

III. COMPUTED RESULTS

In the following, we shall present a selection of the computed results, with particular emphasis on the sensitivity of the findings to the way in which the surface temperature has been evaluated.

A. *Overview of Surface Temperature Effect*

In order to provide a realistic perspective regarding this new approach presented here, it is important to recall some of the earlier work and to compare these previous predictions with those based on the current model.

Figure 3(a) shows the weld pool shape at t = 8.0 s using an approach adopted by Oreper and Szekely,[2] where an upper limit was assigned to the free surface temperature, 2500 K in the particular case cited. The grid configuration is similar to that employed by Oreper and Szekely[2] to allow for direct comparison. Figure 3(b) shows the corresponding weld pool surface temperature. The velocity and penetration plot shown in Figure 3(a) is seen to be in good agreement with previously published results,[2] using identical boundary conditions, but a rather different computational code. This provides proof for the internal consistency of these computed results.

Figure 4 shows the computed temperature for the input conditions calculated from a 200-A arc of a 6.3-mm arc length at a 4-second exposure time. In this instance, the material is assumed to be 2 wt pct Mn steel. Figure 4(a) represents the computed free surface temperature if Langmuir vaporization were invoked, while Figure 4(b) represents the effect of imposing a "ceiling" on the free surface temperature. It is clear that the Langmuir vaporization mechanism would overestimate the rate of heat

Table III. Thermodynamic Properties of Mn and Fe Used in Calculating Surface Temperature[16,21]

Mole Fraction X_{Mn}	Activity a_{Mn}	Partial Excess Free Energy $\overline{\Delta G}^{xs}_{Mn}$ (cal/mole)
0	0	1050
0.1	0.126	851
0.2	0.240	672

$$\log_{10} P^{0}_{Mn}\ (\text{mm Hg}) = \frac{-14{,}520}{T} - 3.02 \log_{10} T + 19.24$$

Mole Fraction X_{Fe}	Activity a_{Fe}	Partial Excess Free Energy $\overline{\Delta G}^{xs}_{Fe}$ (cal/mole)
0	0	1050
0.1	0.126	851
0.2	0.240	672
0.3	0.345	515
0.4	0.443	378
0.5	0.537	263
0.6	0.628	168
0.7	0.718	95
0.8	0.809	42
0.9	0.902	11
1.0	1.000	0

$$\log_{10} P^{0_{Fe}}\ (\text{mm Hg}) = \frac{-19{,}710}{T} - 1.27 \log_{10} T + 13.27$$

Table IV. Composition of AISI 304[19]

AISI 304 Stainless Steel (Composition in Weight Percent)			
0.1	C	8.4	Ni
18.1	Cr	0.040	P
0.33	Cu	0.022	S
0.31	Mn	0.69	Si
0.31	Mo	0.48 V	—
69.928	Fe	—	—

loss from the workpiece. Thus, the actual surface temperature should be even higher than that predicted by Figure 4(a) if mixed control vaporization were invoked at the free surface. Thus, an alternative explanation is needed.

B. *Effect of Surface Tension Coefficient*

It is a well-established fact that thermocapillary motion plays a key role in determining metal circulation in weld pools. This flow is driven by the surface tension gradient, which, in turn, is due to the temperature dependence of the surface tension. It follows that the precise nature of this relationship is of major importance. There is a general agreement that for most steel grades $\partial\gamma/\partial T$ is of the order of 10^{-4} N/m · K;[25] furthermore, it is thought that for pure iron, $\partial\gamma/\partial T$ is negative, while the presence of impurities, such as sulfur, will result in a positive value for $\partial\gamma/\partial T$.

The situation is complicated by the fact that upon raising the temperature of a sulfur-containing melt to a high enough level, the bonds between sulfur and iron will break, and hence, one may expect that $\partial\gamma/\partial T$ will change its sign with temperature. The implications of this behavior on the thermocapillary flows produced is obvious, resulting in rather more complex, multicellular flows.

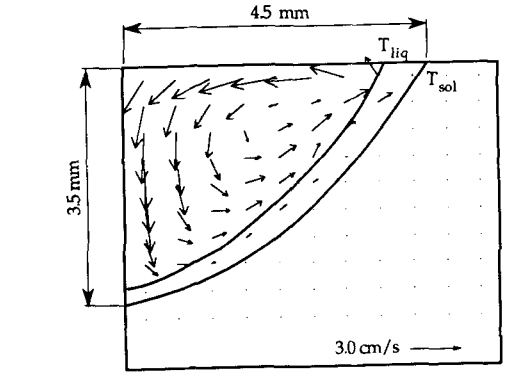

(*a*)

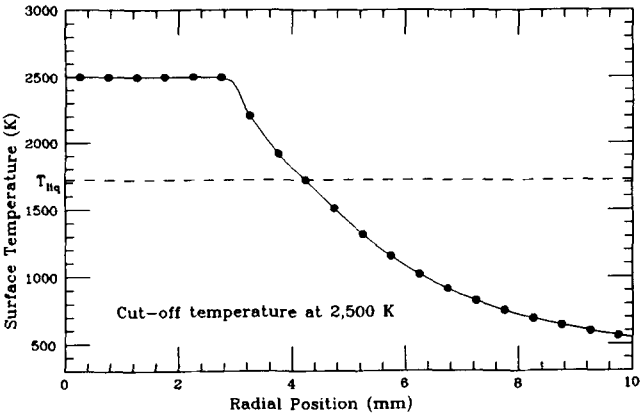

(*b*)

Fig. 3—Calculated (*a*) weld pool flow profile and (*b*) surface temperature distribution due to Oreper and Szekely's[2] boundary conditions.

Sahoo *et al.*[17] have developed a semiempirical model for predicting $\partial\gamma/\partial T$ for binary system. This has been given by Eqs. [35] and [36] and is plotted in Figure 5 for the AISI 304 described in Table IV and an FeS binary alloy. Sahoo *et al.*[17] showed that the critical parameter that controls $\partial\gamma/\partial T$ is the heat of adsorption, ΔH°, and suggested an empirical relationship for estimating ΔH°. Using this technique, ΔH° is estimated as -1.66×10^{8} J/kg · mole for FeS[17]* and -1.88×10^{8} J/kg · mole for AISI 304.[5] Inspection of the $\partial\gamma/\partial T$ plot in Figure 5 shows that $\partial\gamma/\partial T$ is very sensitive to the ΔH° value chosen. The difference in ΔH° is about 10 pct, but the difference in the temperature where $\partial\gamma/\partial T$ changes sign is about 300 K, as shown in Figure 5.

*FeS is considered the stable compound for the temperature range in arc welding operation.[25]

Since the flow field is driven by the surface tension gradient, the need for the precise knowledge of the temperature profile is obvious, especially when the temperatures approach the value at which $\partial\gamma/\partial T$ undergoes a

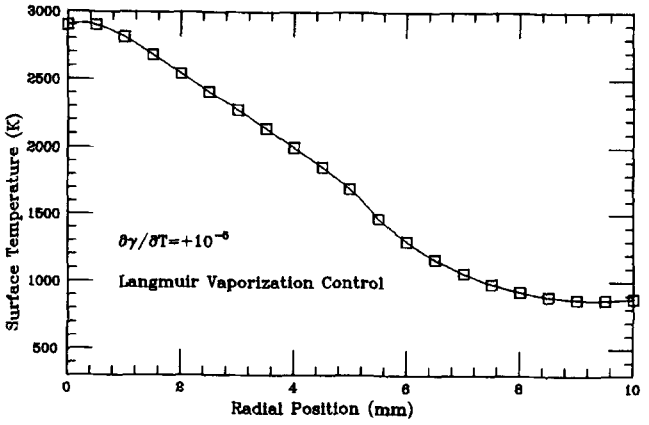

(a)

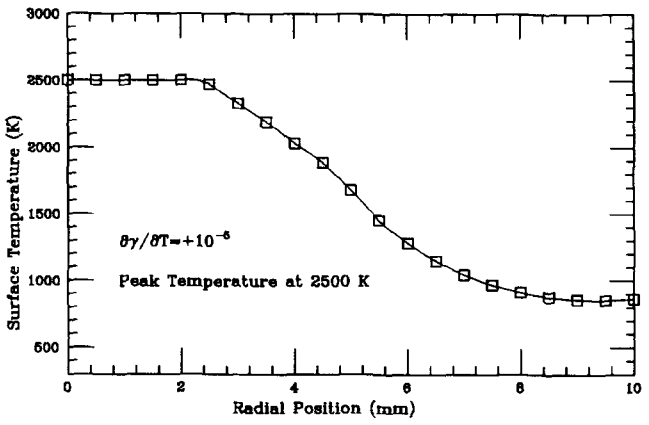

(b)

Fig. 4—Plot of surface temperature due to (*a*) Langmuir vaporization and (*b*) "limiting" peak surface temperature. Sample is for 2 pct Mn-steel.

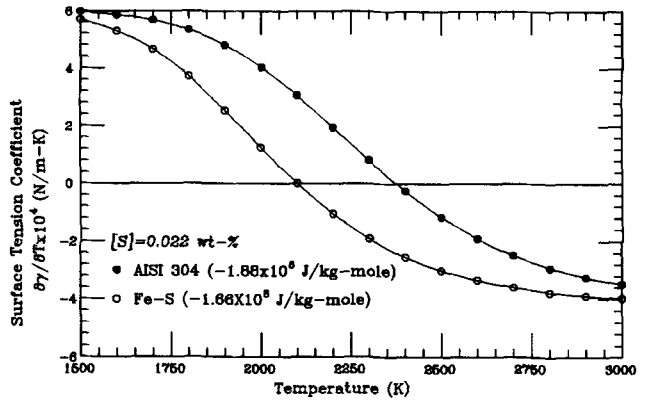

Fig. 5—Surface tension coefficient as a function of temperature for AISI 304 and FeS binary alloy solution with [S] = 0.022 wt pct.[17]

sign change. The complex velocity fields that may result from this change in sign of $\partial\gamma/\partial T$ were first discussed by Zacharia and co-workers;[5,6] however, in their work the heat and current fluxes falling on the weld pool were postulated, rather than computed, from first principles, as is the case here.

All the results that follow implicitly assume $\partial\gamma/\partial T$ as given by Eq. [35] unless otherwise stated.

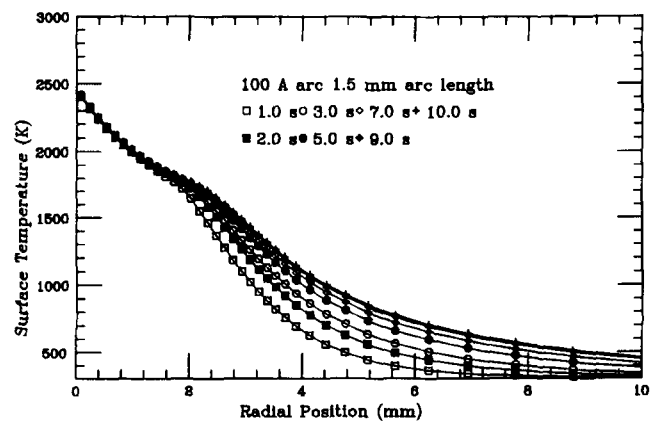

(a)

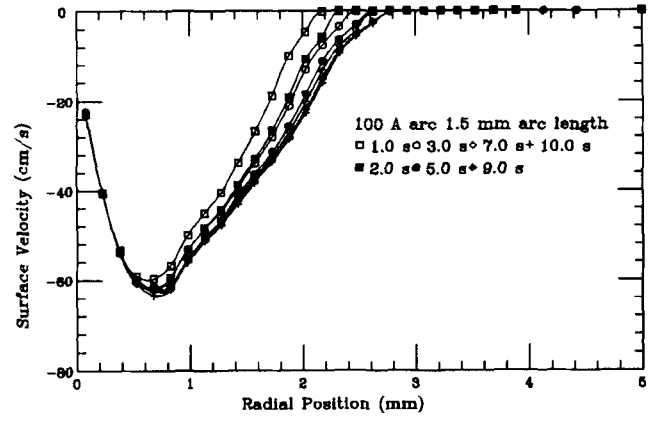

(b)

Fig. 6—Transient development of weld pool of (*a*) surface temperature and (*b*) surface velocity on heating with 100 A (1.5 mm arc length) at 1.0-s intervals. Plot is shown up to 10.0 s.

C. *Computed Results Pertaining to the Experiments by Kraus[19] and Zacharia et al.[20]*

The bulk of the computed results to be presented in the following are aimed at representing the conditions prevailing in the experiments reported by Kraus[19] and Zacharia *et al.*[20] In these experiments, the actual readings were taken after a 25-second interval, at which time steady-state conditions were thought to have been attained; that is, the rate of heat input was exactly balanced by the rate of heat loss.

The computer calculations required a substantial amount of CPU time (about 6 hours of computer time on the APOLLO 10000 for each second of real time); for this reason, we carefully explored the approach to steady state and found that steady state has been reasonably closely approached after the passage of about 5 seconds, and hence, the bulk of the calculations was terminated after the lapse of 5 seconds.

This point is illustrated in Figures 6 through 9; all of these results were calculated using a variable $\partial\gamma/\partial T$, as given by Eq. [35]. Figures 6(a) and (b) show the surface temperature and velocity profile, respectively, while Figure 7 shows the evolution of the weld pool and the circulation pattern, and it is seen that the changes are relatively minor after the passage of about 4 seconds for

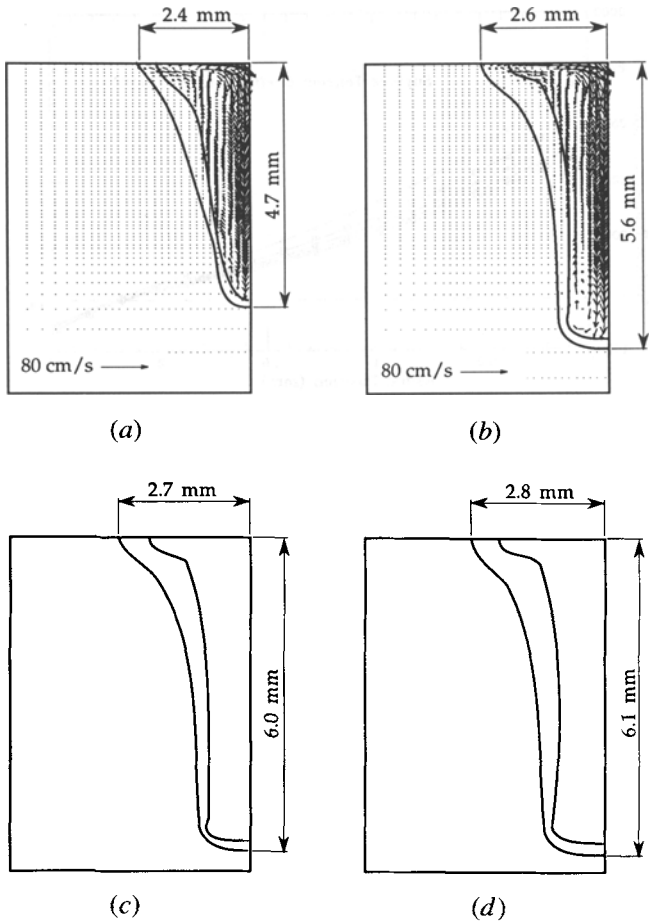

Fig. 7—Velocity profile plots as a function of time corresponding to Fig. 6: (*a*) 2.0 s: T_{max} = 2413 K, u_{max} = 68.3 cm/s; (*b*) 5.0 s: T_{max} = 2417 K, u_{max} = 69.3 cm/s; (*c*) 7.0 s: T_{max} = 2420 K, u_{max} = 68.5 cm/s; and (*d*) 10.0 s: T_{max} = 2420 K, u_{max} = 70.2 cm/s.

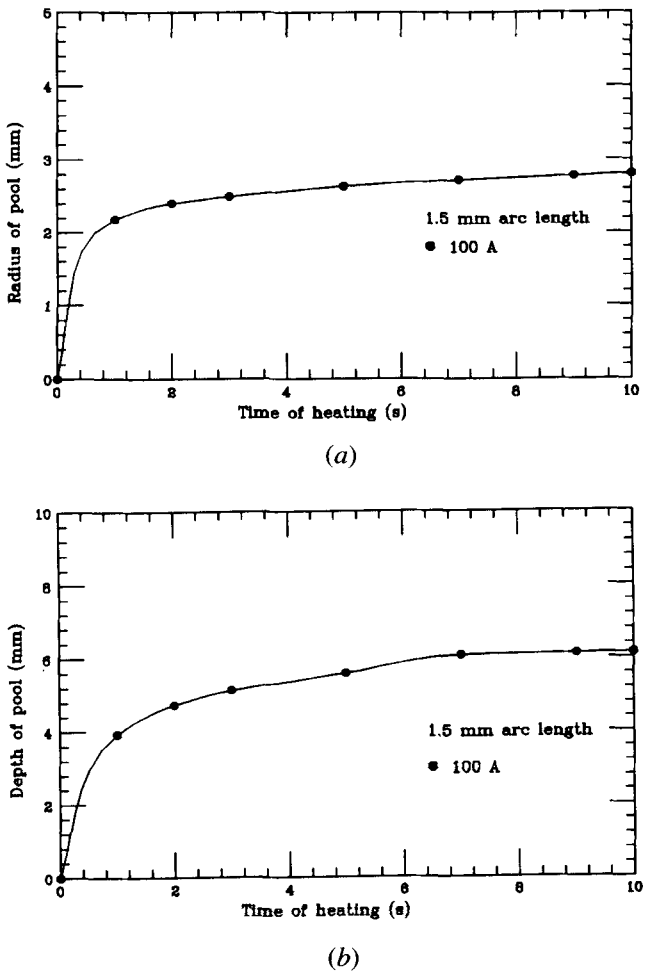

Fig. 8—Transient weld pool size development (*a*) radius and (*b*) depth as a function of time corresponding to Figure 6. The size increases rapidly after the first 2 s and slows thereafter.

the present case. Figures 8(a) and (b) show the evolution of the pool radius and of the pool depth, respectively; these data exhibit a similar trend. Finally, Figure 9 shows the evolution of the maximum pool temperature and of the maximum melt velocity with time, where it is seen that these attain a steady value, even for a much shorter time period. Figure 9(a) is of particular interest, because it shows that by a realistic allowance for thermocapillary flow, one can obtain a realistic limiting temperature for the free surface of the weld pool.

D. *Computed Results with Constant Surface Tension Coefficient*

In view of the considerable uncertainty that exists regarding the precise nature of the relationship between surface tension and temperature, it is of interest to explore the effect of changing the surface tension on the behavior of the system. Figure 10 shows computed values of the surface temperature distribution (after the passage of a 5-second period) with the value of $\partial\gamma/\partial T$ as a parameter. In these calculations, we assumed a constant value for this term. It is seen that for positive value of $\partial\gamma/\partial T$, the peak surface temperatures can be brought down to quite reasonable values, as found in experiments,[19] provided $\partial\gamma/\partial T$ is greater than about 3×10^{-4} N/m·K. When $\partial\gamma/\partial T$ is negative, which should be the case for pure substances, the peak surface temperature will be significantly higher.

Figure 11 shows a plot of the peak surface temperature and of the peak surface velocity against $\partial\gamma/\partial T$; these plots clearly indicate the close (inverse) correlation between the peak velocity and the peak temperature. This is, of course, consistent with physical reasoning, because the recirculating flow field is responsible for dissipating the thermal energy within the system.

The effect of $\partial\gamma/\partial T$ on the temperature and the velocity profiles is examined further in Figure 12, where three sets of curves are presented: one for a constant $\partial\gamma/\partial T$ value of 5×10^{-4} N/m·K, the other for the "standard case" of a variable $\partial\gamma/\partial T$, as deduced from the relationship proposed by Sahoo *et al.*,[17] with the last one representing a 10 pct reduction in the ΔH° value from the standard case.

In examining these plots, three points should be noted. One is that the temperature profiles may markedly depend on the specific form of the relationship between γ and T. The other is the strong correlation between the velocity and the temperature fields. Finally, and perhaps most importantly, there appears to be a threshold velocity (for a given size and energy input, which is about 25

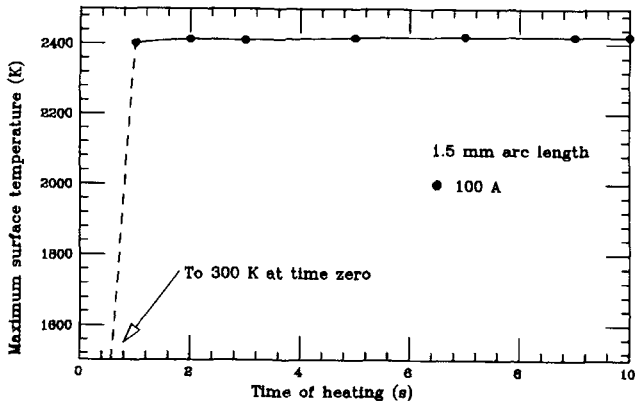

(*a*)

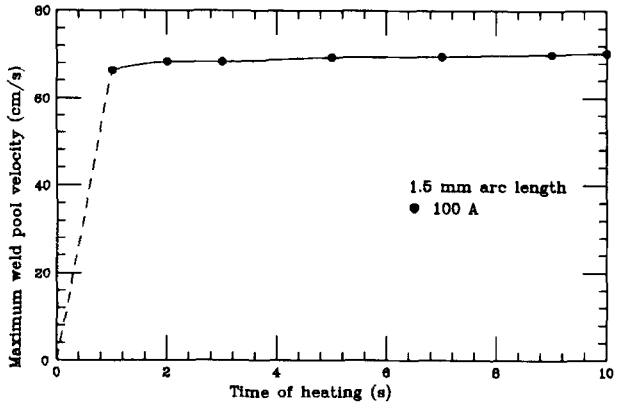

(*b*)

Fig. 9—Maximum (*a*) weld pool surface temperature and (*b*) surface velocity as a function of heating times. It is noted that the maximum value does not change significantly after 2 s.

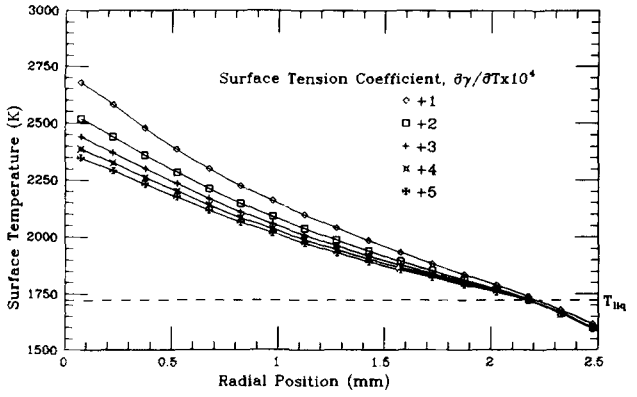

(*a*)

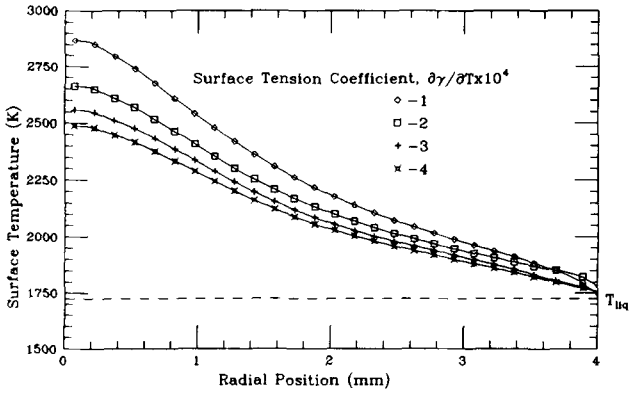

(*b*)

Fig. 10—Plot of surface temperature as a function of radial position for (*a*) positive $\partial\gamma/\partial T$ and (*b*) negative $\partial\gamma/\partial T$.

cm/s for the present case) beyond which the peak temperature is kept within reasonable bounds (*i.e.*, below the boiling point), and the behavior of the system becomes less sensitive to the precise relationship between surface tension and temperature. This appears to be a very important finding, which will be discussed subsequently.

Let us now turn our attention to a critical comparison of the theoretical predictions and the experimental measurements of Kraus[19] and Zacharia *et al.*[20] It is noted that in most previous work aimed at comparing measured and predicted weld pool shapes, the energy input was chosen somewhat arbitrarily and thus could serve as an adjustable parameter. In the present case, the energy input was calculated from first principles.

Figure 13 shows the experimentally measured weld pool profiles for the 100-A arc. The calculated pool profile and velocity field is given in Figure 14, and the very marked disparity is readily apparent. More specifically, the measured profile is relatively broad, while the predicted pool shape is deep and narrow. It is difficult to provide a rational explanation for this discrepancy, because the uncertainties in the temperature-surface tension relationship could not account for this marked change in the pool shape.

The one assumption that needs critical revision is the postulate of laminar flow; if somewhat arbitrarily, we assume mildly turbulent behavior and use "effective" viscosity and thermal conductivity, which are 30 times the atomic value; the resultant profiles show a marked change, as seen in Figure 15. Under these conditions, the weld pool is much broader and the penetration is reduced; thus, the theoretically predicted pool profiles will become much closer to those found experimentally. The preliminary nature of these results has to be stressed. Nonetheless, the computed profiles given in Figure 15 indicate the clear need to critically examine whether the flow in weld pools is laminar. The implications of these findings will be discussed subsequently.

IV. DISCUSSION

The laminar flow model was not able to predict the pool shape that was obtained experimentally. Attention was then drawn to employing turbulent flow *via* constant effective viscosity and thermal conductivity. It was found that as the effective viscosity increased from twice the molecular value to 50 times that value, the pool shape changed from one of deep penetration to a more rounded pool. The pool shape reported in Figure 15 (30 times molecular value) is one that closely resembles the experimental result. Further refinement of the model *via*

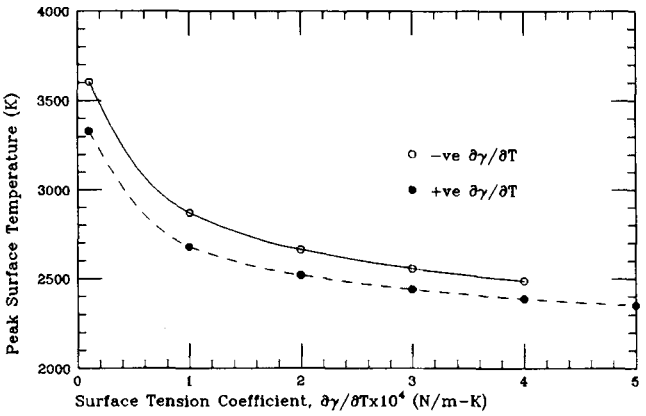

(a)

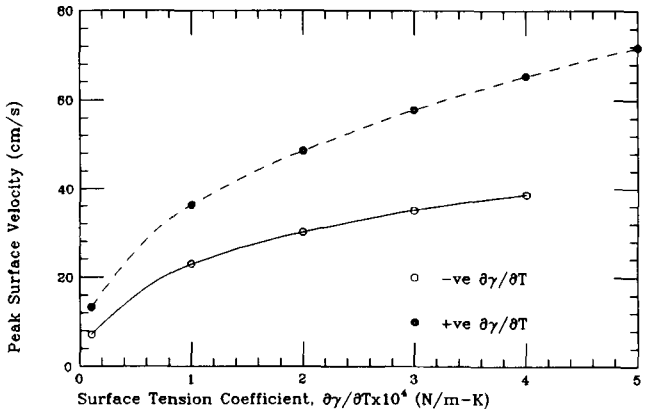

(b)

Fig. 11—Plot of (*a*) peak surface temperature and (*b*) peak surface velocity as function of $\partial\gamma/\partial T$. Plot (a) is derived from Figs. 10(a) and (b).

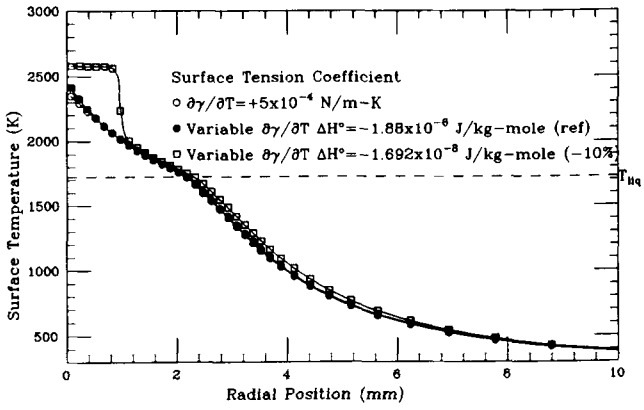

(a)

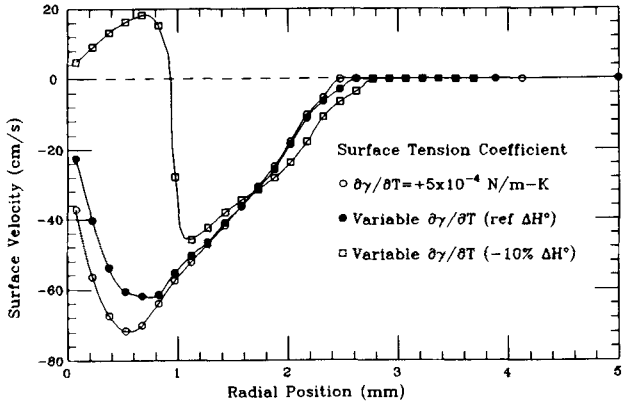

(b)

Fig. 12—Plot of (*a*) surface temperature and (*b*) surface velocity as a function of radial position for $\partial\gamma/\partial T = +5 \times 10^{-4}$ N/m · K and for variable $\partial\gamma/\partial T$ as given by Eq. [35]. The variable $\partial\gamma/\partial T$ consists of two cases, due to different material properties: (1) case 1 with $\Delta H^\circ = -1.88 \times 10^8$ J/kg · mole (ref ΔH°) and (2) case 2 with $\Delta H^\circ = -1.692 \times 10^8$ J/kg · mole (−10 pct ΔH°).

one of the built-in PHOENICS turbulence models will require some modification of those models, as it is suspected that the flow conditions in the weld pool vary from laminar to transitional to turbulent due to the growing pool size.

The analysis assumes that the weld pool surface is flat. This is reasonable in view of the low arc current modeled (100 A). Massive surface depressions (>1 mm) are not expected until higher currents are employed (>240 A).[26] If surface fluctuations are small (≪1 mm), on average, the assumption of a planar free surface seems adequate.

Although the combined arc-weld pool model is a one-way coupling, it is felt that the welding arc is not significantly affected by the weld pool surface conditions. Although Part I[1] discusses the importance of arc length, surface fluctuations are commonly found in GTAW even in low currents. These are, however, dynamic pulsating conditions. Under steady-state conditions and on average, the arc length can be considered constant, and thus, the free surface can be considered planar.

Under these conditions, the pool surface temperature can affect welding arc anode film temperature. In particular, the anode heat flux is affected. There are three contributions to the anode heat flux: (1) electronic transfer (~82 pct), (2) convective transfer (~15 pct), and

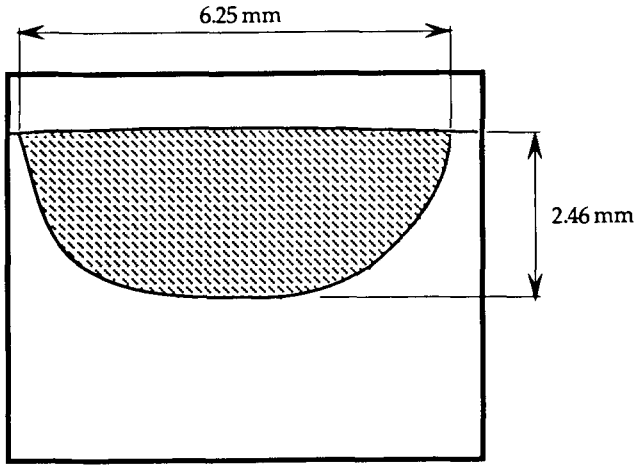

Fig. 13—Experimental weld pool shape due to Zacharia *et al.* (100 A).[20]

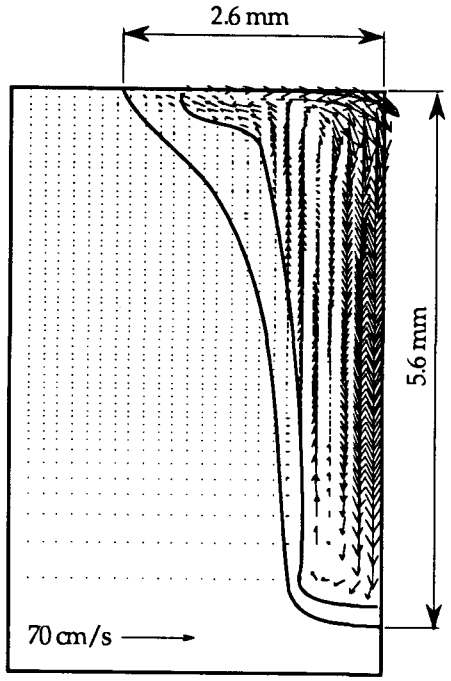

Fig. 14—Calculated weld pool shape and flow profile for laminar physical properties (100 A).

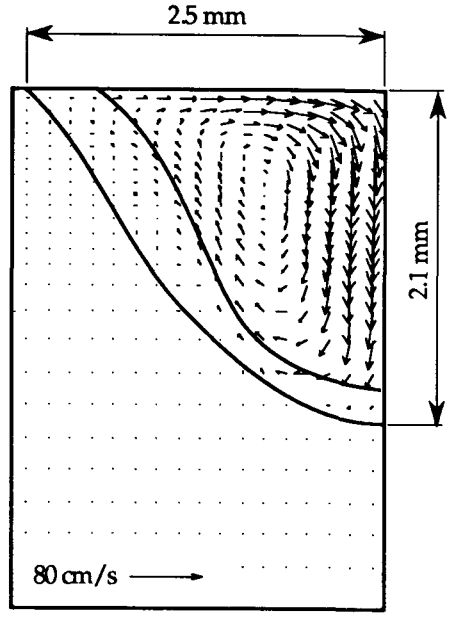

Fig. 15—Weld pool shape and flow profile calculated based on the effective viscosity and thermal conductivity that are 30 times the molecular value (100 A).

(3) radiative transfer (~3 pct). Of these three, only the convective and radiative transfers depend on the weld pool surface temperature. As the radiative contribution is only 3 pct, its contribution is small. The convective contribution requires the pool temperature so as to calculate the film temperature thermophysical and transport properties. The arc temperature spans between 12,000 and 15,000 K over the pool surface. As the pool surface temperature spans only from 1723 K to 2500 K, the effect of the pool temperature on the welding arc film temperature is thus small.

The key advantage in calculating the heat flux from first principles is to reduce the number of empirical constants invoked, in this case, for the heat flux (and also the current flux) which governs convective flow. Another advantage is the determination that vaporization (both Langmuir and mixed control) is not the rate-limiting factor governing peak weld pool surface temperature.

Although Gaussian heat flux is used frequently in modeling studies, one experimental study[27] has indicated that the heat flux is not truly Gaussian but is, in fact, somewhat sharply skewed. In the Gaussian-type distribution, the two main adjustable parameters are the current efficiency and the heat distribution parameter. Although there is general consensus as to the nominal values of these two constants, there remain some uncertainties as to how they vary with factors such as arc length, shielding gas composition, and electrode size and type. Calculating the heat flux from first principles can help overcome some of these difficulties.

It was previously believed that vaporization was the limiting factor to the peak surface temperature. In many cases, Langmuir vaporization was invoked, and the extent of this vaporization was controlled by the adsorption/desorption coefficient. This value is usually not known precisely. There is a further mechanism that controls the vaporization rate, and this is due to the mass transfer (diffusion) of the vapor species across the anode concentration boundary layer of the welding arc. In order to determine this vaporization rate, the temperature at the boundary layer must be known, which can be easily determined if the arc is solved numerically. Since the arc conditions could be calculated (Part I[1]), it was found that vaporization was not the limiting factor to the weld pool peak surface temperature. This observation eventually led to the conclusion that weld pool thermocapillary convection was the principal mechanism limiting free surface temperature.

V. CONCLUDING REMARKS

In this article, we presented computed results describing the pool profiles, the velocity fields, and the temperature fields in weld pools; a key feature of these results was the fact that the heat and current fluxes falling on the free surface of the weld pool were calculated from first principles, rather than assigned arbitrarily.

Novel features of the calculation included a realistic allowance for vaporization and a realistic dependence of the surface tension on temperature. The computed results were quite instructive, because they provided some new, hitherto unavailable insights into weld pool behavior. The principal findings may be summarized as follows:

1. Vaporization from the weld pool surface is not a major component in the overall heat balance and in itself cannot account for the experimental observation that the maximum free surface temperature of weld pools usually does not exceed about 2700 K.
2. The principal mechanism that appears to limit the free surface temperature is thermocapillary convection.

3. Thermocapillary motion is expected to depend critically on the precise nature of the relationship between the temperature and surface tension. This fact would seem to introduce quite serious complications, because $\partial\gamma/\partial T$ will change sign at about 2400 K for the present case. The physicochemical explanation for this behavior is quite simple; below this temperature, impurities such as sulfur will cause the surface tension to increase with increasing temperature, while above this threshold value and upon approaching the boiling point of the workpiece, the surface tension will decrease with increasing temperature.
4. From a practical standpoint, one of the most important findings was that once a critical surface velocity is exceeded (say about 25 cm/s in the present case), the precise nature of the relationship between temperature and surface tension became rather less important in determining the maximum temperature that may be attained by the system. In a physical sense, the reason for this behavior is the fact that the temperature gradients and the surface velocities are closely interrelated, with high velocities tending to diminish the temperature gradients. This may explain the experimental observations that welding results are not that critically sensitive to relatively minor changes in the operating conditions.
5. Perhaps the most intriguing, while still somewhat preliminary, finding of this work has been that the computed results could not predict the experimentally observed weld pool shapes. However, quite good qualitative agreement could be obtained between measurements and predictions, if one postulated turbulent behavior and enhanced both the viscosity and the thermal conductivity of the melt by a factor of about 30. Under these conditions, the weld pool shapes become rather more rounded, in good apparent agreement with observations. This latter aspect of the problem deserves a great deal of further attention.

LIST OF SYMBOLS

a_i	activity of i (—)
$a_{i(T)}$	activity of i at temperature T (—)
$a_{i(T_{ref})}$	activity of i at reference temperature T_{ref} (—)
A	constant in surface tension coefficient (N/m · K)
B_θ	azimuthal magnetic field (Wb/m^2)
C_p	heat capacity (J/kg)
$\overline{C_p}$	integral mean heat capacity (J/kg)
C_i^s	concentration of i at surface of workpiece (kg/m^3)
C_i^∞	concentration of i in the bulk of shielding gas (kg/m^3)
$D_{Mn\text{-}Ar}$	binary diffusion coefficient of Mn in Ar gas (m^2/s)
E	electric potential field (V/m)
f_L	fraction of fluid in mushy zone (—)
g	gravitational acceleration (m/s^2)
h_e	plasma enthalpy at the edge of the boundary layer (J/kg)
h_{heat}	heat-transfer coefficient at workpiece surface (W/m^2 · K)
$h_{L,i}$	Langmuir transfer coefficient due to vaporization of species i (W/m^2 · K)
h_{mass}	mass-transfer coefficient (m/s)
$h_{m(eff)}$	effective mass-transfer coefficient (m/s)
$h_{m(eff),i}$	effective mass-transfer coefficient of species i (m/s)
h_{vap}	mass-transfer coefficient due to vaporization (m/s)
h_w	plasma enthalpy at the anode wall (J/kg)
I	arc current (A)
J	current density [vector quantity] (A/m^2)
J_a	anode current flux (A/m^2)
J_c	cathode spot current density (A/m^2)
J_0	current density flux at $r = 0$ (A/m^2)
J_r	radial current density (A/m^2)
J_z	axial current density (A/m^2)
k	thermal conductivity (W/m · K)
k_1	entropy of segregation (—)
k_b	Boltzmann constant (J/K)
k_{liq}	thermal conductivity of liquid steel (W/m · K)
k_{sol}	thermal conductivity of solid steel (W/m · K)
K	drag coefficient in source term for phase change (kg/m^{3}s)
K_{seg}	equilibrium constant for segregation (—)
K_{max}	maximum drag coefficient in phase change term (kg/m^{3}s)
L_r	radius of plate (m)
L_z	thickness of plate (m)
$L_{vap,i}$	heat of vaporization of i (J/kg)
$m_{L,i}$	mass flux of species i due to Langmuir vaporization (kg/m^2 · s)
m_i	mass flux of Fe due to vaporization of species i (kg/m^2 · s)
M_i	atomic weight of i (kg/mole)
n_{Le}	index in Lewis number (—)
Nu_w	Nusselt number at the anode wall (—)
P	pressure (Pa)
P_i	partial pressure of i (Pa)
$P_{i(T)}$	partial pressure of i at temperature T (Pa)
P_i^0	vapor pressure of pure i (Pa)
Pr	Prandtl number $C_p\mu/k$ (—)
Pr_w	plasma Prandtl number at the anode wall temperature $C_p\mu/k$ (—)
q	heat flux (W/m^2)
q_a	anode heat flux (W/m^2)
$q_{L,i}$	heat loss of species i by Langmuir vaporization (W/m^2)
q_{net}	net heat input into workpiece (W/m^2)
q_0	heat flux at $r = 0$ (W/m^2)
$q_{vap,i}$	heat loss due to vaporization of species i (W/m^2)
$q_{vap,tot}$	total heat loss from anode due to vaporization and mass transfer (W/m^2)
r	radial direction (m)
r_{ij}	the direction vector from surface S_i to volume element V_j (m)
R	gas constant (J/g · mole)
Re_w	Reynolds number at the anode wall (—)
Sc	Schmidt number, $\nu/D_{Mn\text{-}Ar}$ (—)
S_R	radiation source (W/m^3)
T	temperature (K)

$T_{bp(Ar)}$ boiling point of argon (K)
T_e plasma temperature at the edge of the boundary layer (K)
T_{liq} liquidus temperature (K)
T_{max} maximum pool temperature (K)
$T_{mp(i)}$ melting point of i (K)
T_r reference temperature for Boussinesq approximation (1523 K)
T_{ref} reference temperature in activity calculations (K)
T_s surface temperature of workpiece (K)
T_{sol} solidus temperature (K)
T_w wall temperature (K)
t time (s)
u radial velocity (m/s)
u_e radial velocity at the edge of the boundary layer (m/s)
u_{max} maximum pool velocity (m/s)
V arc voltage (V)
w axial velocity (m/s)
x fraction of power increment (—)
X_i mole fraction of i (—)
z axial coordinate (m)

Greek Symbols

α thermal diffusivity (m^2/s)
α_j current distribution parameter (m^{-1})
α_q heat distribution parameter (m^{-2})
β volume coefficient of thermal expansion (K^{-1})
γ surface tension (N/m)
Γ_s surface excess at saturation ($kg/mole \cdot m^2$)
$\partial\gamma/\partial T$ surface tension coefficient ($N/m \cdot K$)
ΔH^{xs}_{Mn} partail excess free energy of Mn in binary Fe-Mn alloy (cal/mole)
ΔH latent heat of fusion of steel (J/kg)
ΔH° standard heat of adsorption ($J/kg \cdot mole$)
θ azimuthal direction (radian)
μ dynamic viscosity ($kg/m \cdot s$)
μ_b dynamic viscosity at the anode temperature ($kg/m \cdot s$)
μ_e dynamic viscosity of shielding gas at the edge of the boundary layer ($kg/m \cdot s$)
μ_{liq} dynamic viscosity of liquid steel ($kg/m \cdot s$)
μ_0 magnetic permeability of free space (H/m)
μ_w dynamic viscosity of shielding gas at the anode wall ($kg/m \cdot s$)
ν kinematic viscosity (m^2/s)
ρ density (kg/m^3)
$\rho_{bp(Ar)}$ density of argon at boiling point (kg/m^3)
ρ_c charge density (C/m^3)
ρ_e density of shielding gas at the edge of the boundary layer (kg/m^3)
ρ_r reference density for Boussinesq approximation (7200 kg/m^3)
ρ_w density of shielding gas at the anode wall (kg/m^3)
σ_b Stefan-Boltzmann constant ($W/m^2 \cdot K^4$)
σ_e electric conductivity $(ohm \cdot m)^{-1}$
τ_{st} surface tension (Marangoni) shear stress (Pa)
ϕ electric potential (V)

ACKNOWLEDGMENTS

The authors wish to thank the United States Department of Energy, Basic Energy Sciences Section, for financial support of this investigation under Grant No. DE-FG02-87ER45289. The use of the Apollo DN 10000 Supercomputer, which has been donated by Apollo Computer Inc. to the MIT Materials Processing Center, is gratefully acknowledged.

REFERENCES

1. R.T.C. Choo, J. Szekely, and R.C. Westhoff: *Metall. Trans. B*, 1992, vol. 23B, pp. 357-69.
2. G.M. Oreper and J. Szekely: *Metall. Trans. A*, 1987, vol. 18A, pp. 1325-32.
3. T. Zacharia, A.H. Eraslan, D. Aidun, and S.A. David: *Metall. Trans. B*, 1989, vol. 20B, pp. 645-59.
4. T. Zacharia, A.H. Eraslan, and D.K. Aidun: *Weld. J.*, 1988, vol. 67, pp. 53s-62s.
5. T. Zacharia, S.A. David, J.M. Vitek, and T. DebRoy: *Weld. J.*, 1989, vol. 68, pp. 499s-509s.
6. T. Zacharia, S.A. David, J.M. Vitek, and T. DebRoy: *Weld. J.*, 1989, vol. 68, pp. 510s-519s.
7. S. Kou and Y.H. Wang: *Weld. J.*, 1986, vol. 65, pp. 63s-70s.
8. *FLOW-3D: Computational Modelling Power for Scientists and Engineers*, Document FSI-88-00-1, Flow Science, Inc., Los Alamos, NM, 1988.
9. J. Szekely: *Fluid Flow Phenomena in Metals Processing*, Academic Press, New York, NY, 1979, pp. 178-85.
10. R.T.C. Choo and J. Szekely: *Weld. J.*, 1992, vol. 71, pp. 77s-93s.
11. A. Block-Bolten and T.W. Eagar: *Metall. Trans. B*, 1984, vol. 15B, pp. 461-69.
12. J. McKelliget and J. Szekely: *Metall. Trans. A*, 1986, vol. 17A, pp. 1139-48.
13. W.M. Rosenhow and J.P. Hartnett: *Handbook of Heat Transfer*, McGraw-Hill, New York, NY, 1973, pp. 8-126.
14. J.G. Marvin and G.S. Deiwert: *Convective Heat Transfer in Planetary Gases*, NASA Tech. Rept. R-224, 1965.
15. R.B. Bird, W.E. Stewart, and E.N. Lightfoot: *Transport Phenomena*, John Wiley, New York, NY, 1960, pp. 508-13.
16. R. Hultgren, P.D. Desai, D.T. Hawkins, M. Gleiser, and K.K. Kelley: *Selected Values of Thermodynamic Properties of Binary Alloys*, ASM, Metals Park, OH, 1973.
17. P. Sahoo, T. DebRoy, and M.J. McNallan: *Metall. Trans. B*, 1988, vol. 19B, pp. 483-91.
18. O.H. Nestor: *J. Appl. Phys.*, 1962, vol. 33, pp. 1638-48.
19. H.G. Kraus: *Weld. J.*, 1989, vol. 68, pp. 269s-279s.
20. T. Zacharia, S.A. David, J.M. Vitek, and H.G. Kraus: Metals and Ceramics Division, Oak Ridge National Laboratory, Oak Ridge, TN, unpublished research, 1990.
21. R.T.C. Choo, J. Szekely, and R.C. Westhoff: *Weld. J.*, 1990, vol. 66, pp. 346s-361s.
22. R.C. Westhoff: S.M. Thesis, Massachusetts Institute of Technology, Cambridge, MA, 1989.
23. D.B. Spalding: *J. Mathematics and Computers in Simulation*, 1981, vol. XIII, p. 267.
24. S.V. Patankar: *Numerical Heat Transfer and Fluid Flow*, Hemisphere Publishing Corp., Washington, DC, 1980.
25. D.W. Walsh and W.F. Savage: *Weld J.*, 1985, vol. 64, pp. 59s-62s.
26. M.L. Lin and T.W. Eagar: *Weld. J.*, 1985, vol. 64, pp. 163s-169s.
27. M. Lu and S. Kou: *Weld. J.*, 1988, vol. 67, pp. 29s-34s.